Engineering thermal rectification in MoS$_2$ nanoribbons: a non-equilibrium molecular dynamics study†

Leonardo Medrano Sandonas,[abc] Rafael Gutierrez,*[ac] Arezoo Dianat[ac] and Giovanni Cuniberti[acd]

Phononics in two-dimensional (2D) materials is an emergent field with a high potential impact from the basic as well as applied research points of view. Thus it is crucial to provide strategies to control heat flow *via* atomic-scale engineering of the materials. In this study, thermal diodes made of single layer MoS$_2$ nanoribbons are investigated using non-equilibrium classical molecular dynamics. Specifically, we focus on the influence of shape asymmetries of the nanoribbons on the thermal current, and obtain thermal rectification ratios up to 30% for the T-shaped nanoribbons. This behavior is then rationalized through a detailed analysis of the vibrational spectrum of the ribbons. In particular, it turns out that thermal rectification is mostly related to (i) the transversal finite size of the ribbon and (ii) to the different localization behavior of high-frequency modes for forward and backward heat flow directions. We expect our results to shed light on the potential of 2D materials for the engineering of highly efficient nanoscale thermal devices.

1 Introduction

Over the last years, the field of phononics, aiming at controlling heat flow in tailored structures as well as developing thermal devices such as diodes, transistors, and thermal logic gates, has experienced an accelerated progress.[1–4] As a result, novel applications in the fields of nanomachines, electronics, refrigeration, energy harvesting, and energy generation have been suggested.[5,6] In order to carry these ideas into thermal device design, several theoretical and experimental studies have been performed over different length scales, *e.g.* the first solid-state active three-terminal thermal device based on VO$_2$ with large rectification of the heat current has recently been demonstrated.[7] Other successful experimental findings are thermal rectifiers based on carbon or boron-nitride nanotubes, with asymmetric mass loading,[8] and reduced graphene oxide.[9] A thermal rectifier should provide a large heat flow for a certain temperature gradient, but ideally be insulating when the direction of the gradient, and thus that of the heat flow, is reversed. From a theoretical point of view, it has been found that thermal rectification in nanostructured systems sensitively depends on several parameters such as heat bath features,[10,11] the device geometry,[12,13] and on the interface properties between different materials inside the device.[14–17] A common conclusion from these studies is that the simplest mechanism to induce thermal rectification in confined nanoscale systems is to introduce structural asymmetries.

Most of these investigations have focused on carbon-based nanomaterials like carbon nanotubes and graphene nanoribbons.[4,12,13,18–20] In particular, graphene has drawn much attention due to its extremely high thermal conductivity.[21] Besides graphene, however, there are meanwhile a variety of novel two-dimensional (2D) materials like transition metal dichalcogenides, boron nitride (BN), phosphorene, and silicine, which are expected to display different electrical and thermal properties due to the differences in their chemical composition, and thus offer a new broad playground to explore and develop nanoscale devices with tailored electrical, optical, and thermal properties. In particular, molybdenum disulphide (MoS$_2$) has recently attracted considerable interest in the construction of field effect transistors (FET) and optical devices due to its sizable electronic band gap;[22,23] also its potential thermoelectric performance has been highlighted.[24] Although a variety of theoretical studies have been published, addressing the phonon dispersion and thermal conductivity of MoS$_2$ layers and ribbons,[25–38] less attention has so far been devoted to the possibility of *engineering* the thermal response of MoS$_2$ nanostructures *via* structural asymmetries.

[a]Institute for Materials Science and Max Bergmann Center of Biomaterials, TU Dresden, 01062 Dresden, Germany. E-mail: rafael.gutierrez@nano.tu-dresden.de; Fax: +49 (0)351 4633 1422; Tel: +49 (0)351 4633 1419

[b]Max Planck Institute for the Physics of Complex Systems, 01187 Dresden, Germany

[c]Dresden Center for Computational Materials Science (DCCMS), TU Dresden, 01062 Dresden, Germany

[d]Center for Advancing Electronics Dresden, TU Dresden, 01062 Dresden, Germany

† Electronic supplementary information (ESI) available. See DOI: 10.1039/c5ra05733g

Here, we study MoS_2 nanoribbons with strong structural asymmetries by using non-equilibrium molecular dynamics simulations of the thermal transport. We show that thermal rectification ratios of up to 30% can be achieved depending on the degree of asymmetry of the ribbons and rationalize our findings by analyzing in detail the vibrational structure of the systems. This includes an analysis of the mode localization in the nanoribbon, an issue which has been indicated to strongly influence thermal rectification in asymmetric or defective nanostructures made of a single material.[12,39] We find out that different degrees of spatial localization of high-frequency modes for forward and backward heat flow directions are an important factor in determining thermal rectification. We remark that nanostructures such as those investigated here may be already accessible to state-of-the-art experimental approaches. Here, quasi one-dimensional MoS_2 nanoribbons have been successfully synthesized[40] as well as triangular and hexagonal MoS_2 nanoplatelets.[41,42]

2 System and methodology

The atomic structure of a symmetric MoS_2 nanoribbon is shown in Fig. 1a, while Fig. 1b displays three different geometrical shapes for MoS_2 nanoribbons, which we will consider to study possible thermal rectification effects: T-shaped, trapezoidal, and triangular nanoribbons. To quantify the degree of structural asymmetry of these nanostructures, the dimensionless quantity $W_{LR} = W_{Left}/W_{Right}$ is introduced. Here, W_{Left} and W_{Right} are the widths of the left and right ends of the nanoribbon, respectively, and the case of $W_{LR} = 1.0$ corresponds to a fully symmetric rectangular structure.

Non-equilibrium molecular dynamics (NEMD) simulations were carried out by using the LAMMPS code.[43] One crucial issue is the choice of the appropriate force field, since parametrizations developed for bulk systems may in general not be transferable to nanoribbons. In the case of MoS_2, several force fields have recently been developed.[32,33,44] However, they turned out to have different problems when applied to the simulation of

systems with open boundary conditions, such as nanoribbons, at room temperature. Therefore, after careful checks, we have used in our investigation a force field developed on the basis of tight-binding quantum chemistry calculations by Onodera et al.,[45] which includes ionic, covalent, and van der Waals interactions among Mo and S atoms. This interatomic potential has already been successfully applied to study mechanical[45,46] and thermal[35] properties of monolayer MoS_2.

In our simulations, we have considered asymmetric MoS_2 nanoribbons with free boundary conditions in all directions. We have fixed the ends in the X-direction (one layer) to avoid global rotations of the system during the simulation. The standard velocity Verlet algorithm was used to integrate Newton's equations of motion, and the MD time step was set to 0.5 fs. All investigated nanostructures were initially relaxed using a quickstep method. The lattice constant for MoS_2 obtained after relaxation is $a = 3.38$ Å. Equilibration runs for 2 ns and at $T_0 = 300$ K were first performed in the NVT ensemble with a Nosé–Hoover thermostat using a relaxation time equal to 0.1 ps. The choice of a thermostat is a sensitive issue in NEMD simulations, but as discussed in ref. 10, different algorithms in NEMD simulations only led to negligible differences in the computed heat flows (see the ESI† for a discussion of the thermostat parameters used in our simulations). Once the temperature reached the required value, the thermostat was removed, and the NEMD simulations were carried out for 20 ns. The temperatures for left and right heat baths were defined as $T_L = (1 + \alpha)T_0$ and $T_R = (1 - \alpha)T_0$ for the forward direction of the heat flux (heat flows left-to-right or wider-to-narrower) and the opposite case for the backward direction (heat flows right-to-left or narrower-to-wider). We consider as temperature bias $\Delta T = |T_L - T_R| = 2\alpha T_0$ $(\alpha > 0)$. Each heat bath extended over four atomic layers corresponding to a length of roughly 2.3 nm. Time averages of the temperature and the heat current were carried out over the last 10 ns of the simulation. The temperature profile was then computed by dividing the system into a certain number of slabs and using the relation: $T_i = \dfrac{1}{3N_i k_B} \sum_{k=1}^{N_i} m_k v_k^2$,

where N_i is the number of atoms in the ith slab, and m_k and v_k correspond to the atomic mass and velocity of atom number k, respectively. Furthermore, the calculated temperature for each slab, T_i, was averaged over a predefined time interval to obtain a smooth temperature profile. To avoid spurious effects related to the specific choice of initial velocities, an average over five random choices of the initial velocity distribution was additionally performed. To quantify the efficiency of thermal transport in both temperature bias directions, a thermal rectification (TR) ratio η can be defined as:

$$\eta[\%] = \left(\frac{|J_f - J_b|}{J_b} \right) \times 100, \tag{1}$$

where the subscripts indicate whether the rectifier is operated in the forward or backward direction of the heat flux. The heat currents $J_{f,b}$ induced by the temperature bias ΔT are computed as $J_{f,b} = (\partial E_{Left}^{f,b}/\partial t + \partial E_{Right}^{f,b}/\partial t)/2$, where $E_{Left}^{f,b}$ and $E_{Right}^{f,b}$ are the total energies that have been added to or subtracted from the
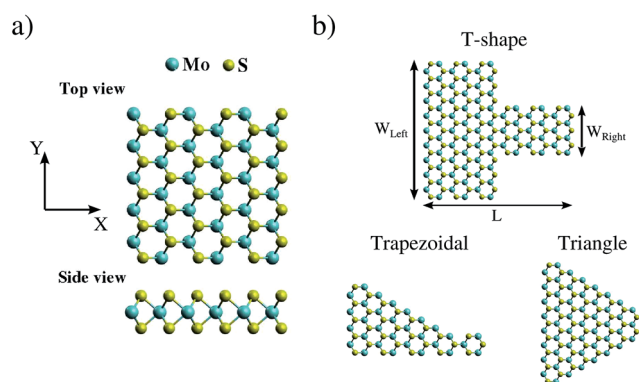

Fig. 1 (a) Schematic of monolayer MoS_2. Top and side views in the armchair direction. (b) Asymmetric geometrical shapes selected for our MoS_2 nanoribbons. We consider $W_{Left} = \sqrt{3}L/2$. The asymmetry degree is measured by the $W_{LR} = W_{Left}/W_{Right}$ parameter.

atoms in the left (L) and right (R) heat baths, respectively. It is worth noting that once the system reaches the steady state, the absolute values of the time derivatives has to be almost the same for the left and right baths. As it is discussed in the ESI,† a wrong choice of thermostat parameters may lead to an improper interpretation of the simulation results.

3 Results and discussion

In Fig. 2a we show the temperature profile for $\alpha = 0.1$, for trapezoidal MoS$_2$ nanoribbons of length $L = 5.9$ nm ($W_{\text{Left}} = \sqrt{3}L/2$) with $W_{\text{LR}} = 1.0$ (symmetric) and $W_{\text{LR}} = 3.0$ (asymmetric). For symmetric nanoribbons, the temperature profile has a symmetric and nearly linear behavior for both directions, forward and backward, of the applied temperature bias, so that no rectification of the thermal current can take place, as expected. On the contrary, for $W_{\text{LR}} = 3.0$, the temperature gradient along the nanoribbon becomes non-linear and displays a different dependence on the spatial distance from the heat baths for forward and backward heat flows. Notice also that the mean temperature is mainly controlled by the wider heat bath (left bath), and this shows up in the strong non-linear evolution of the temperature profile with increasing distance from the wider bath. As a result of the asymmetric temperature profiles for both temperature bias directions, the corresponding thermal currents are also different and heat rectification can take place, see Fig. 2b. In other words, the heat flux runs preferentially from the wider to the narrower region, so that the device behaves as a "good" thermal conductor in that direction. This behavior is improved when the temperature bias is increased, as shown in the inset of Fig. 5. In Fig. 2c, the TR ratio η is displayed as a function of the geometrical asymmetry parameter W_{LR}. For the different nanoribbon shapes, the qualitative trends are rather similar: with increasing structural asymmetry, the degree of rectification increases and can achieve rather high values of roughly 30%, values which are comparable with those found in more complex engineered graphene nanoribbons.[12,20] This behavior is related to the increasing difference in the number of atoms involved in the nanoribbon–heat bath interaction at both ends with increasing W_{LR}, which

increasingly breaks the heat flux symmetry as the temperature bias is reversed. Similar effects have been reported for graphene ribbons.[12,13,18] There is however a clear quantitative difference in the heat rectification efficiency of the T-shaped ribbons when compared to the triangular and trapezoidal ones, namely, the former has a larger TR ratio for the same length L. This is largely related to how the transition from the wider to the narrower region is built in: in the triangular and trapezoidal nanoribbons, the transition is smooth (we may call it adiabatic as done with quantum point contacts[47]), while for the T-shaped ribbon there is a narrow interface region where an abrupt transition from wider to narrower sections takes place. Thus, heat flow differences resulting from the global asymmetry of the nanoribbon will be enhanced due to this sharp interface. We also notice that upon increasing the system size, the effect of the structural asymmetry in thermal rectification weakens and eventually disappears, i.e. $\eta \to 0$ for L(or W) $\to \infty$. This tendency is illustrated for the T-shaped ribbons with two different lengths: $L = 5.9$ nm and $L = 9.4$ nm (see Fig. 2c) and highlights the fact that, besides structural asymmetry, another major factor influencing thermal rectification is the transversal finite size of the nanostructures. This has been previously discussed in carbon-based nanostructures.[1,12,13]

To rationalize the process of thermal rectification in asymmetrically structured MoS$_2$ nanoribbons, we have performed a real-space mode analysis.[48] For the sake of clarity, we focus on the T-shaped nanoribbon with $L = 5.9$ nm and $W_{\text{LR}} = 3.0$, since the results for the other geometries are qualitatively similar. Fig. 3a shows the total and partial vibrational density of states (PVDOS) of the T-shaped ribbon. The PVDOS is defined as:[49]

$$g_A(\omega) = \sum_{j_A} \sum_\lambda \sum_\alpha |\varepsilon_{j_A\alpha,\lambda}|^2 \delta(\omega - \omega_\lambda), \quad (2)$$

where $\varepsilon_{j_A\alpha,\lambda}$ is the vibrational eigenvector component of mode λ with a polarization $\alpha = X, Y, Z$, and ω_λ is the frequency of the corresponding mode. Notice that the sum over j_A only includes atoms of a given type (A = Mo or A = S). Summing then over the index A gives the total VDOS. We notice that these quantities are computed by first diagonalizing the dynamical matrix of the last configuration of a given NEMD run, and then performing an average over several runs differing by the initial conditions
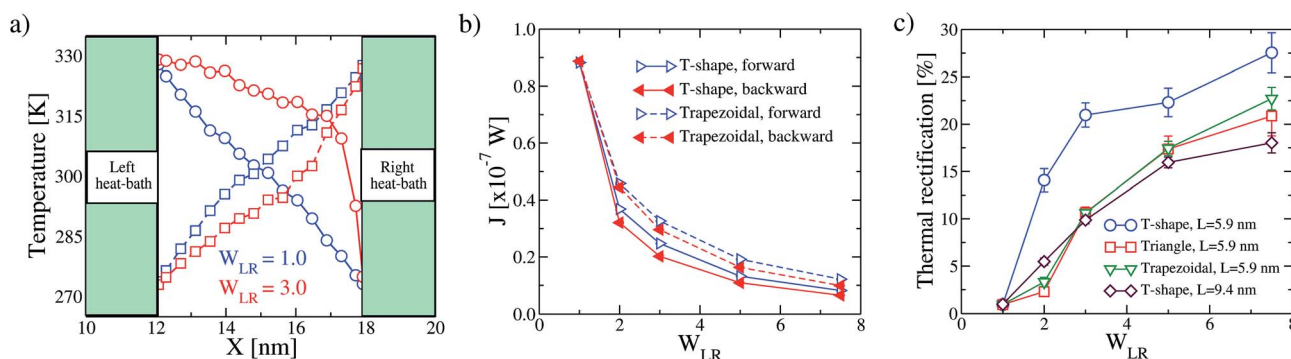

Fig. 2 (a) Temperature profile for trapezoidal nanoribbons of length equal to 5.9 nm with $W_{\text{LR}} = 1.0$ (blue lines) and $W_{\text{LR}} = 3.0$ (red lines). Both, forward (○) and backward (□) directions of the heat flux are shown. Variation of the (b) heat flux and (c) thermal rectification after increasing the W_{LR} parameter for each geometrical shape. For these calculations, we have considered $T_0 = 300$ K and $\alpha = 0.1$.
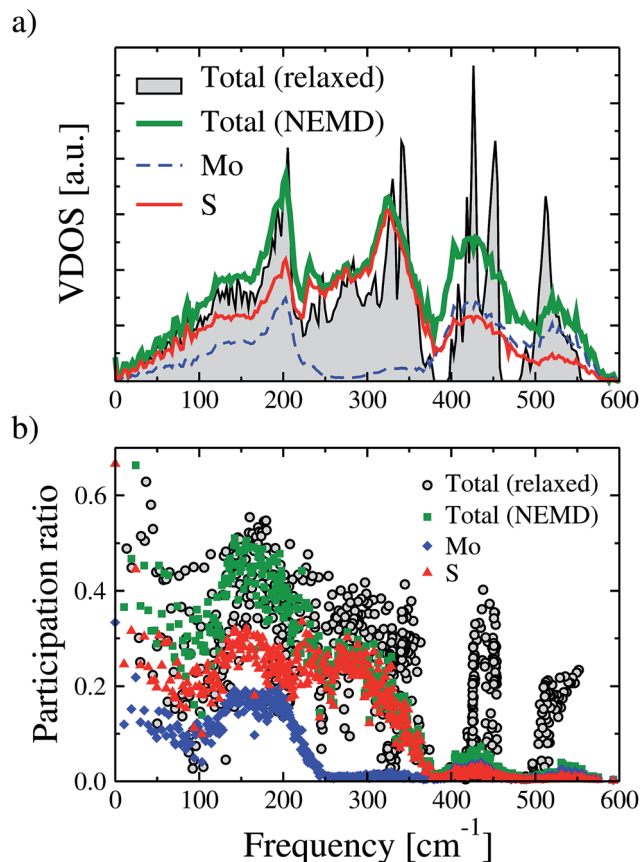
a)

b)

Fig. 3 Total and partial vibrational density of states (a) and participation ratio (b) for the T-shaped MoS_2 nanoribbon with length $L = 5.9$ nm and $W_{LR} = 3.0$ as obtained from NEMD simulations in the forward temperature bias direction ($\alpha = 0.1$). For reference, we also show the corresponding total VDOS for the structurally relaxed (i.e. before starting the NEMD simulation) T-shaped MoS_2 nanoribbon with $W_{LR} = 3.0$.

(velocities), as previously mentioned (see also additional details in the ESI†).

In Fig. 3a, we also show as reference the VDOS of the structurally relaxed T-shaped nanoribbon before running the NEMD simulation (black solid line). The major difference to the VDOS obtained from the NEMD simulation (green solid line) is the spectral broadening, which manifests more clearly for the high-frequency vibrational modes above 400 cm^{-1}. Looking now at the PVDOS for the two atom types in the nanoribbon, Mo and S, we can roughly identify three different spectral regions:[32] a low frequency range (up to 200 cm^{-1}) where both S and Mo atoms carry similar spectral weights, although the contributions of the S atoms are slightly larger; an intermediate range ($\sim$200–380 cm^{-1}), where the spectral weight is carried almost exclusively by S atoms; a high frequency range (>380 cm^{-1}) where again both atom types contribute similarly to the total VDOS, although here Mo atoms have a slightly larger spectral weight. For the backward heat flow direction a similar qualitative behavior was obtained (not shown). The information provided by the VDOS analysis does not reveal the degree of localization or delocalization of the vibrational modes in different spectral ranges.

Hence, to characterize each mode λ with respect to these features, the participation ratio (PR) has been calculated, which is defined according to:

$$p_\lambda^{-1} = N \sum_i \left(\sum_\alpha \varepsilon_{i\alpha,\lambda}^* \varepsilon_{i\alpha,\lambda} \right)^2 \qquad (3)$$

Here, $\varepsilon_{i\alpha,\lambda}$ is the vibrational eigenvector component of atom i and N is the number of atoms in the system. The PR measures the fraction of atoms participating in a mode and hence varies between 1.0 for delocalized modes to O(1/N) for localized modes. The PR is displayed in the lower panel of Fig. 3. We also show as a reference, similar to the VDOS plot in Fig. 3a, the PR for the T-shaped relaxed nanoribbon previous to starting the NEMD simulation. Additionally, partial PRs separately associated to the sulfur and molybdenum atoms are shown. Partial PRs are obtained by restricting the summation over the atom index i in eqn (3) to only atoms of a given type.[50]

The first point to notice is that the non-equilibrium vibrational spectrum is mostly modified in the higher frequency part with modes lying roughly above 400 cm^{-1}. While for the relaxed nanoribbon two clear groups of modes in this spectral range with PR $\sim$ 0.4 and 0.25 can be identified, the non-equilibrium modes show a considerably larger degree of localization with PR below 0.1. For lower frequencies the differences between these two cases are much weaker, though. The partial PRs show that modes with a higher degree of delocalization (larger PR) involve in general a larger contribution from sulfur atoms. In general terms, apart from the very low frequency vibrations below 100 cm^{-1} and a narrow region between 150 cm^{-1} and 220 cm^{-1}, almost all modes in the nanoribbon display a stronger tendency to localization with PRs smaller than 0.4, which is a signature of the strong impact of the structural asymmetries, finite cross-section of the nanoribbons, and temperature. It is worth mentioning that, based on their polarization vector, the atoms are essentially vibrating in-plane during the NEMD simulation, but this behavior depends on the specific frequency of the vibrational mode (see the ESI† for additional details).

To complement the previous analysis, the spatial distribution of the vibrational modes located within a specific spectral range (Λ) was analyzed by defining the quantity $\phi_{i\alpha,\Lambda}$, which is computed as:[39]

$$\phi_{i\alpha,\Lambda} = \frac{\sum_{\lambda \in \Lambda} \varepsilon_{i\alpha,\lambda}^* \varepsilon_{i\alpha,\lambda}}{\sum_{1 \leq j \leq N} \sum_{\lambda \in \Lambda} \varepsilon_{j\alpha,\lambda}^* \varepsilon_{j\alpha,\lambda}} \qquad (4)$$

A large value of $\phi_{i\alpha,\Lambda}$ indicates a strong contribution of the ith atom to vibrational modes belonging to the spectral region defined by Λ. To define the set Λ, three possible PR regions were selected, as shown in the central panel of Fig. 4: (I) $p > 0.4$, (II) $0.1 < p < 0.4$, and (III) $p < 0.1$. The behavior of $\phi_{i\alpha,\Lambda}$ for domains I and II turned out to be almost the same for forward and backward heat flows and we show these results in the ESI.† Hence, the modes in those spectral ranges do not seem to strongly determine the rectification of the heat current. Major
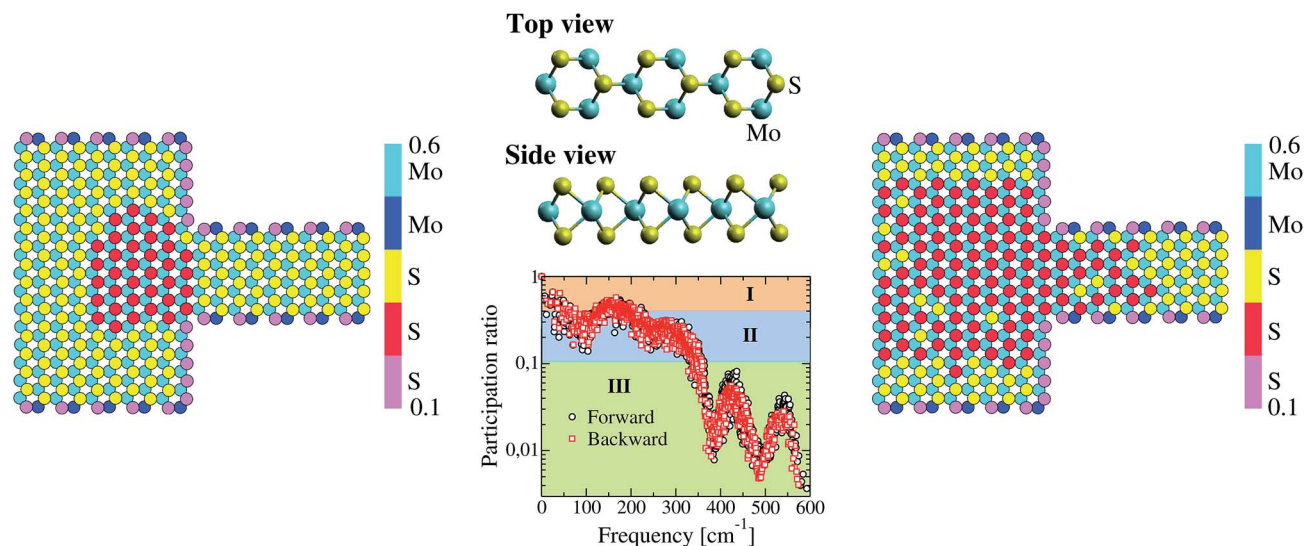
Fig. 4 Spatial distributions, ϕ, of the vibrational modes for the T-shaped MoS$_2$ nanoribbons of $L = 5.9$ nm and $W_{LR} = 3.0$ (XY plane). We only have considered the vibrational modes with $p < 0.1$ (see region III in the central panel) for the system obtained after the NEMD simulation in the forward (left panel) and backward (right panel) directions. directions of the heat flux ($\alpha = 0.1$). The color scale has the same meaning for all the cases, *i.e.*, the cyan balls mean highest contribution while the pink balls mean lowest contribution for the vibrational modes. In these pictures, we only show the contributions arising from the top S-layer as well as the Mo-layer.

differences were however found for region III as displayed in the left and right panels of Fig. 4. At this point, we need to make a remark concerning the graphical representation of the spatial distribution of the vibrational modes. In contrast to other 2D materials, which consist of a single atomic layer like graphene or BN, the MoS$_2$ nanoribbon is made of three atomic layers. This makes the visualization of the quantity $\phi_{i\alpha,\Lambda}$ more involved. We have however found, by analyzing the contribution of each atomic layer separately, that the two sulfur planes contribute in similar ways to the spatial distribution of the

modes, something to be expected for symmetry reasons. Hence, we only show in Fig. 4 the contributions arising from the top S-layer as well as from the Mo-layer. The left and right panels of Fig. 4 illustrate the spatial distribution for the modes in region III for the forward (left panel) and backward (right panel) directions. The main observed feature is the strong increase, in the backward flow direction, in the number of atoms giving a low contribution (0.2–0.3) to the modes in spectral region III, *i.e.* for frequencies above 350 cm^{-1}. This behavior mainly affects a set of atoms in the bulk of the nanoribbon, while atoms along the edges do not appreciably change the degree of their contribution to the selected spectral range. Moreover, we find that sulfur atoms are those mostly influenced upon reversal of the heat flow, while the contribution from Mo atoms is considerably less modified and remains relatively high ($\phi_{i\alpha,\Lambda} > 0.5$). A simple mathematical relationship between the degree of spatial localization of the vibrational modes and the heat current as computed in a NEMD run is difficult to establish. In this sense, our results only hint at the fact that the strong modification in the spatial distribution of certain groups of modes upon reversal of the direction of heat current flow in *asymmetric* nanostructures is a major factor determining the size of the thermal rectification effect found in the structurally asymmetric MoS$_2$ nanoribbons. This conclusion is however further supported by a corresponding analysis carried out for the trapezoidal shaped nanoribbons, which show a very similar behavior (see the ESI†): a strong modification in the mode spatial distribution over the inversion of the heat current flow. To this effect, which has also been highlighted in earlier works on graphene nanoribbons,[11,12] one also needs to add, as mentioned previously, the finite transversal size of the ribbons, which modifies the boundary conditions for the vibrational spectrum as well as its localization properties, and thus also
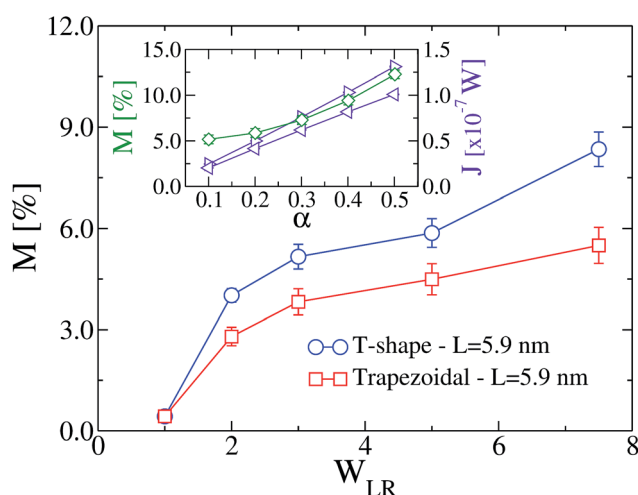

Fig. 5 Dependence of the M parameter on the asymmetry degree, W_{LR}, for the T-shaped and trapezoidal MoS$_2$ nanoribbons. We only show the values obtained by considering frequencies with $p < 0.1$. Inset: variation of the M parameter ($\diamond$) and heat flux ($\triangleright$ – forward and $\triangleleft$ – backward direction) after increasing the temperature bias for the T-shaped nanoribbon with $W_{LR} = 3.0$.

strongly determines the heat transport features of the system. Clearly, these factors – asymmetry, finite size, mode localization – are not independent from each other and their interplay induces the observed rectification features in the MoS_2 nanoribbons.

Lastly, to round off our discussion and to provide a better illustration of the influence of the lateral confinement on the thermal rectification, we have introduced the parameter:

$$M[\%] = \left(\frac{|\Pi_f - \Pi_b|}{\Pi_b}\right) \times 100, \qquad (5)$$

where $\Pi = \langle p \rangle_\lambda$ is a frequency averaged participation ratio and the λ modes belong to a specified spectral range Λ. We have found that, as expected from the previous discussion, the average participation ratios in the forward and backward directions for the spectral ranges I and II defined above are almost identical, implying $M \sim 0$. Thus, Fig. 5 only shows the dependence of M on the W_{LR} parameter corresponding to case III with $p < 0.1$ for the T-shaped and trapezoidal MoS_2 nanoribbons. Similar to the behavior of the thermal rectification factor η, M increases when the nanoribbon becomes more asymmetric and consistently, the effect is stronger for the T-shaped ribbon. Finally, the inset of Fig. 5 suggests that another alternative to increase the rectification ratio is to enhance the applied temperature bias, as has been reported for other systems.[10,12,13]

4 Conclusions

We have performed classical non-equilibrium molecular dynamics simulations to address thermal rectification effects in structurally asymmetric MoS_2 nanoribbons. As a result of our study, the T-shaped nanoribbons displayed the largest rectification ratio (up to 30%), when compared with the trapezoidal and triangular structures, thus illustrating the strong sensitivity of thermal transport to the specific design of the lateral confinement. Our results clearly indicate that the thermal rectification effect is related to (i) shape asymmetries and (ii) changes in the degree of spatial localization of high-frequency modes (frequencies larger than 350 cm^{-1}) under non-equilibrium heat transport conditions. Due to the more complex atomic structure of the MoS_2 nanoribbons, we may expect that atomic-scale engineering, e.g. of the nanoribbon edges, will open broad possibilities for tailoring the thermal response of the systems. This goes, however, beyond the scope of the current study.

Acknowledgements

References

1 N. Li, J. Ren, L. Wang, G. Zhang, P. Hänggi and B. Li, Rev. Mod. Phys., 2012, 84, 1045–1066.

2 M. Maldovan, Nature, 2013, 503, 209–217.

3 H. Han, L. G. Potyomina, A. A. Darinskii, S. Volz and Y. A. Kosevich, Phys. Rev. B: Condens. Matter Mater. Phys., 2014, 89, 180301.

4 W.-R. Zhong, D.-Q. Zheng and B. Hu, Nanoscale, 2012, 4, 5217–5220.

5 A. A. Balandin and D. L. Nika, Mater. Today, 2012, 15, 266–275.

6 J. Gomis-Bresco, D. Navarro-Urrios, M. Oudich, S. El-Jallal, A. Griol, D. Puerto, E. Chavez, Y. Pennec, B. Djafari-Rouhani, F. Alzina, A. Martnez and C. S. Torres, Nat. Commun., 2014, 5, 1–6.

7 J. Zhu, K. Hippalgaonkar, S. Shen, K. Wang, Y. Abate, S. Lee, J. Wu, X. Yin, A. Majumdar and X. Zhang, Nano Lett., 2014, 14, 4867–4872.

8 C. W. Chang, D. Okawa, A. Majumdar and A. Zettl, Science, 2006, 314, 1121–1124.

9 H. Tian, D. Xie, Y. Yang, T.-L. Ren, G. Zhang, Y.-F. Wang, C.-J. Zhou, P.-G. Peng, L.-G. Wang and L.-T. Liu, Sci. Rep., 2012, 2, 523.

10 J. Lee, V. Varshney, A. K. Roy, J. B. Ferguson and B. L. Farmer, Nano Lett., 2012, 12, 3491–3496.

11 T. S. Komatsu and N. Ito, Phys. Rev. E: Stat., Nonlinear, Soft Matter Phys., 2010, 81, 010103.

12 Y. Wang, A. Vallabhaneni, J. Hu, B. Qiu, Y. P. Chen and X. Ruan, Nano Lett., 2014, 14, 592–596.

13 N. Yang, G. Zhang and B. Li, Appl. Phys. Lett., 2009, 95, 033107.

14 W. Kobayashi, Y. Teraoka and I. Terasaki, Appl. Phys. Lett., 2009, 95, 171905.

15 A. K. Vallabhaneni, B. Qiu, J. Hu, Y. P. Chen, A. K. Roy and X. Ruan, J. Appl. Phys., 2013, 113, 064311.

16 J. Lan and B. Li, Phys. Rev. B: Condens. Matter Mater. Phys., 2006, 74, 214305.

17 Y. Chalopin and S. Volz, Appl. Phys. Lett., 2013, 103, 051602.

18 J. Hu, X. Ruan and Y. P. Chen, Nano Lett., 2009, 9, 2730–2735.

19 Q.-X. Pei, Y.-W. Zhang, Z.-D. Sha and V. B. Shenoy, Appl. Phys. Lett., 2012, 100, 101901.

20 G. Zhang and H. Zhang, Nanoscale, 2011, 3, 4604–4607.

21 X. Xu, L. F. C. Pereira, Y. Wan, J. Wu, K. Zhang, X. Zhao, S. Bae, C. T. Bui, R. Xie, J. T. L. Thong, B. H. Hong, K. P. Loh, D. Donadio, B. Li and B. Özyilmaz, Nat. Commun., 2014, 5, 3689.

22 R. Kappera, D. Voiry, S. E. Yalcin, B. Branch, G. Gupta, A. D. Mohite and M. Chhowalla, Nat. Mater., 2014, 1128–1134.

23 B. Radisavljevic, A. Radenovic, J. Brivio, V. Giacometti and A. Kis, Nat. Nanotechnol., 2011, 6, 147–150.

24 J. Wu, H. Schmidt, K. K. Amara, X. Xu, G. Eda and B. Özyilmaz, Nano Lett., 2014, 14, 2730–2734.

25 H. Babaei, J. M. Khodadadi and S. Sinha, Appl. Phys. Lett., 2014, 105, 193901.

26 D. D. Fan, H. J. Liu, L. Cheng, P. H. Jiang, J. Shi and X. F. Tang, *Appl. Phys. Lett.*, 2014, **105**, 133113.

27 T.-H. Liu, Y.-C. Chen, C.-W. Pao and C.-C. Chang, *Appl. Phys. Lett.*, 2014, **104**, 201909.

28 D. Wickramaratne, F. Zahid and R. K. Lake, *J. Chem. Phys.*, 2014, **140**, 124710.

29 J.-W. Jiang, X. Zhuang and T. Rabczuk, *Sci. Rep.*, 2013, **3**, 2209.

30 Y. Cai, J. Lan, G. Zhang and Y.-W. Zhang, *Phys. Rev. B: Condens. Matter Mater. Phys.*, 2014, **89**, 035438.

31 W. Li, J. Carrete and N. Mingo, *Appl. Phys. Lett.*, 2013, **103**, 253103.

32 V. Varshney, S. S. Patnaik, C. Muratore, A. K. Roy, A. A. Voevodin and B. L. Farmer, *Comput. Mater. Sci.*, 2010, **48**, 101–108.

33 J.-W. Jiang, H. S. Park and T. Rabczuk, *J. Appl. Phys.*, 2013, **114**, 064307.

34 J.-W. Jiang, *Nanoscale*, 2014, **6**, 8326–8333.

35 X. Liu, G. Zhang, Q.-X. Pei and Y.-W. Zhang, *Appl. Phys. Lett.*, 2013, **103**, 133113.

36 M. Buscema, M. Barkelid, V. Zwiller, H. S. J. van der Zant, G. A. Steele and A. Castellanos-Gomez, *Nano Lett.*, 2013, **13**, 358–363.

37 Q. H. Wang, K. Kalantar-Zadeh, A. Kis, J. N. Coleman and M. S. Strano, *Nat. Nanotechnol.*, 2012, **7**, 699–712.

38 R. Yan, J. R. Simpson, S. Bertolazzi, J. Brivio, M. Watson, X. Wu, A. Kis, T. Luo, A. R. Hight Walker and H. G. Xing, *ACS Nano*, 2014, **8**, 986–993.

39 J. Chen, G. Zhang and B. Li, *Nano Lett.*, 2010, **10**, 3978–3983.

40 Z. Wang, H. Li, Z. Liu, Z. Shi, J. Lu, K. Suenaga, S.-K. Joung, T. Okazaki, Z. Gu, J. Zhou, Z. Gao, G. Li, S. Sanvito, E. Wang and S. Iijima, *J. Am. Chem. Soc.*, 2010, **132**, 13840–13847.

41 J. V. Lauritsen, J. Kibsgaard, S. Helveg, H. Topsoe, B. S. Clausen, E. Laegsgaard and F. Besenbacher, *Nat. Nanotechnol.*, 2007, **2**, 53–58.

42 J. Kibsgaard, J. V. Lauritsen, E. Lgsgaard, B. S. Clausen, H. Topse and F. Besenbacher, *J. Am. Chem. Soc.*, 2006, **128**, 13950–13958.

43 S. Plimpton, *J. Comput. Phys.*, 1995, **117**, 1–19.

44 J. A. Stewart and D. E. Spearot, *Modell. Simul. Mater. Sci. Eng.*, 2013, **21**, 045003.

45 T. Onodera, Y. Morita, A. Suzuki, M. Koyama, H. Tsuboi, N. Hatakeyama, A. Endou, H. Takaba, M. Kubo, F. Dassenoy, C. Minfray, L. Joly-Pottuz, J.-M. Martin and A. Miyamoto, *J. Phys. Chem. B*, 2009, **113**, 16526–16536.

46 T. Onodera, Y. Morita, R. Nagumo, R. Miura, A. Suzuki, H. Tsuboi, N. Hatakeyama, A. Endou, H. Takaba, F. Dassenoy, C. Minfray, L. Joly-Pottuz, M. Kubo, J.-M. Martin and A. Miyamoto, *J. Phys. Chem. B*, 2010, **114**, 15832–15838.

47 B. J. van Wees, H. van Houten, C. W. J. Beenakker, J. G. Williamson, L. P. Kouwenhoven, D. van der Marel and C. T. Foxon, *Phys. Rev. Lett.*, 1988, **60**, 848–850.

48 L. Zhu and B. Li, *Sci. Rep.*, 2014, **4**, 4917.

49 A. Bodapati, P. K. Schelling, S. R. Phillpot and P. Keblinski, *Phys. Rev. B: Condens. Matter Mater. Phys.*, 2006, **74**, 245207.

50 P. K. Schelling and S. R. Phillpot, *J. Am. Chem. Soc.*, 2001, **84**, 2997–3007.